Silicon (2023) 15:1913–1923
https://doi.org/10.1007/s12633-022-02148-x

ORIGINAL PAPER

Structure and Upconversion Luminescence Properties of Pr^{3+}-Doped Y_2SiO_5 Phosphor

Fengqin Lai[1,2] · Xinning Xu[1] · Junwei Shen[1] · Yuhang Wang[1] · Yinuo Yan[1] · Yawen Nie[1] · Weixiong You[1,3] · Di Wu[4] · Lei Han[1,3,4,5] · Zongliang Xiao[1]

Received: 11 August 2022 / Accepted: 28 September 2022 / Published online: 5 October 2022
© Springer Nature B.V. 2022

Abstract
Ultraviolet-C light has significant application prospects in the fields of disinfection, air purification, etc. Herein, an effective UVC upconversion phosphor Y_2SiO_5:Pr^{3+} was successfully prepared, as evidenced by the XRD results. The diffuse reflection spectra of Y_2SiO_5: Pr^{3+} phosphors presented two distinct absorption bands corresponding to the electron transitions of $^3H_4 \rightarrow {}^3P_2$ and $^3H_4 \rightarrow {}^1D_2$, and the E_g was determined to be 4.22 eV for the Y_2SiO_5 host, which is very close to the E_g (4.172 eV) calculated by DFT. Under the excitation of 460 nm laser, two emission peaks centered at ~247 nm and ~258 nm were found in the range of 230-280 nm, which are attributed to the transitions of $4f5d \rightarrow {}^3H_4$ and $4f5d \rightarrow {}^3H_5$ of Pr^{3+} ions. With the help of temperature-dependent emission spectra, the phosphor demonstrated impressive thermal stability up to 150 °C. These findings indicate that the Y_2SiO_5: Pr^{3+} phosphor has the potential application in disinfection.

Keywords Y_2SiO_5: Pr^{3+} phosphor · Upconversion luminescence · Ultraviolet-C · DFT calculation

1 Introduction

Ultraviolet (UV) light is a significant component of sunlight and is closely related to the life activities of humans, animals, and plants on the earth. Despite the fact that UV light is invisible to the human eye, it has demonstrated promising applications in the fields of disinfection, air purification, skin phototherapy, photodynamic therapy, secret communication, as well as optical locating and tracking [1–5]. UV light can be divided into UVA light (320 ~ 400 nm), UVB light (280 ~ 320 nm), and UVC light (200 ~ 280 nm) according to its wavelength [6]. Among them, only UVA and UVB can penetrate the ozone layer and cloud layers to reach the earth's surface, however, these wavelengths are useless germicidal UV radiation because they are beyond the range of microorganisms' absorption maxima. UVC light has a strong bactericidal effect, and its wavelength is in the region of the absorption peaks of microorganisms, which can effectively destroy the structure of microorganisms [7].

The traditional commercial UVC light source is generally the mercury lamp, which has several drawbacks including high power consumption, large heat generation, short lifetime, and potential safety hazards. The performance of semiconductor UVC LEDs is superior to that of mercury lamps and they have the benefits of energy saving, environmental protection, portability, etc. [8]. The practical use and commercialization of this technology are, however, severely constrained by several technological obstacles in supporting apparatus, epitaxial growth, packaging, testing, etc.,

Fengqin Lai and Xinning Xu contributed equally to this work and should be considered co-first authors.

✉ Lei Han
hl89119924@jxust.edu.cn

✉ Zongliang Xiao
xiaozongliang@jxust.edu.cn

1 Faculty of Materials Metallurgy and Chemistry, Jiangxi University of Science and Technology, Ganzhou 341000, China

2 School of Mechanical and Electrical Engineering, Jiangxi University of Science and Technology, Ganzhou 341000, China

3 College of Rare Earths, Jiangxi University of Science and Technology, Ganzhou 341000, China

4 National Engineering Research Center for Ionic Rare Earth, Ganzhou 341000, China

5 Nation Rare Earth Functional Materials Innovation Centre, Ganzhou 341000, China

resulting in low luminous efficiency of UVC-LEDs, poor heat dissipation, and low lifetime.

Upconversion luminescence is a process in which the long-wavelength light is converted into short-wavelength light, such as the luminescence of Pr^{3+}/Yb^{3+} co-doped La_2O_3 and $La(OH)_3$ nano-phosphors [9], Yb^{3+}/Pr^{3+} co-doped Y_2O_3 phosphors [10], and Yb^{3+}/Pr^{3+} co-doped $Sr_3Al_2O_6$ phosphors [11], etc. UV upconversion luminescent materials are a class of hosts that can convert long-wavelength light into short-wavelength UV light [12, 13], and their characteristic of converting low-energy light into high-energy light has achieved practical applications in many fields such as solid-state lasers, sterilization, and photomedicine [14]. In the past few years, UV upconversion luminescence is mainly realized by exciting luminescent ions with high energy density near-infrared lasers, and the luminescent ions usually absorb three or more near-infrared photons in this process [15]. In the process of multiphoton UV upconversion luminescence, the intermediate energy level of rare earth ions will experience energy loss of non-radiative transition, resulting in very low upconversion luminescence efficiency for the material [14]. However, the efficiency of the two-photon UV upconversion luminescence process, which is driven by visible light, may be significantly increased by typically only requiring one intermediate energy level. At present, UV upconversion emission under visible light excitation has been reported in Er^{3+}-doped luminescent materials through excitation state absorption and energy transfer process. Qin et al. [16] discovered the UV upconversion emission in the Er^{3+}-doped Y_2O_3 phosphor excited by a 532 nm continuous wave compact solid-state laser. Detailed discussions and arguments show that there are energy transfer upconversion and excited state reabsorption processes, which play an extremely important role in the population of the $^4D_{5/2}$ level and $^2P_{3/2}$ level. In addition to Er^{3+} ion, Pr^{3+} ion may likewise generate highly efficient UVC emission through the $4f5d$ excited state level, and the $4f \rightarrow 4f5d$ transition exhibits stronger visible light absorption characteristics. For example, Yin et al. [17] studied upconversion luminescence from visible light to UVC light in $Li_2SrSiO_4:Pr^{3+}$ phosphors. It has a maximal emission power of 0.25 mW/cm^2 and can effectively inactivate bacteria within 10 minutes, which proves that the synthesized $Li_2SrSiO_4:Pr^{3+}$ phosphor is a kind of efficient UV phosphor. Additionally, Wu et al. [18] noted UVC upconversion emission in $LiYF_4:Pr^{3+}$ microcrystal and investigated the dependence between the 488 nm laser excitation density and emission intensity during the UVC upconversion process. The results show that the two-photon process plays an important role in UVC upconversion emission, and this UVC phosphor offers a wide range of potential applications in the field of sterilization. Here, yttrium orthosilicate (Y_2SiO_5) is considered to be a promising host material for a variety of applications in phosphors, fiber amplifiers, anti-counterfeiting technology, laser technology, optical information storage due to its high thermal stability, good chemical stability, and optical properties, as well as simple preparation process [19]. Meanwhile, the trivalent Pr^{3+} ion has a good energy level structure and a long excited-state lifetime, which enables it to continuously absorb two photons and thus transit to a lower energy state to obtain high-energy photons [20]. As a result, Pr^{3+}-doped Y_2SiO_5 will be an effective UV upconversion phosphor.

In this work, a series of Y_2SiO_5: Pr^{3+} phosphors were successfully synthesized by the solid-state reaction method. The crystal structure, morphology, diffuse reflection spectra, emission spectrum, and temperature-dependent emission spectra of the phosphors were also meticulously investigated.

2 Experimental Section

2.1 Materials and Sample Synthesis

All raw materials of SiO_2 (Macklin, ≥ 99.99%), Y_2O_3 (Macklin, ≥ 99.99%), and Pr_2O_3 (Macklin, ≥ 99.9%) were used without additional purification.

The undoped Y_2SiO_5 (YSO) and Pr^{3+} doped $Y_{2-x}SiO_5$: xPr^{3+} (YSO: xPr^{3+}, $x = 0.04$, 0.08, 0.12, 0.16, and 0.20) phosphors were successfully prepared by using the high-temperature solid-state reaction method. To be more precise, stoichiometric mixtures of SiO_2, Y_2O_3, and Pr_2O_3 were ground for 30 minutes in the agate mortar. Then, the homogeneous mixtures were transferred into the alundum crucible and placed into an electric furnace. Finally, the mixed powders were sintered at 1500 ~ 1650 °C for 6 hours. The calcined products were ground into fine powder for further characterization.

2.2 Characterization and Theoretical Calculation

The XRD patterns of the prepared powders were obtained using the X-ray diffractometer (Bruker D8 Advance) with Cu $K\alpha$ radiation at 40 kV and 40 mA. The crystallographic structure of phosphor was fitted by the GSAS software [21]. The crystal morphology and elemental mapping of phosphors were recorded by SEM (Carl Zeiss, Germany) and EDS detector (Oxford Aztec Standard X-MaxN 20 mm^2). The diffuse reflection spectra (DRS) of $Y_{2-x}SiO_5$: xPr^{3+} phosphors were obtained via a UV-Vis-NIR spectrophotometer (PerkinElmer Lambda 950). The fluorescence spectra of $Y_{2-x}SiO_5$: xPr^{3+} phosphors were realized using the fluorescence spectrometer (FLS 980, Edinburgh Instruments, UK) equipped with a 460 nm solid-state laser as an excitation source. The density functional theory (DFT) calculation was conducted by the Material Studio package [22]. The Perdew-Burke-Ernzerhof (PBE) generalized-gradient approximation

(GGA) was applied to describe the exchange-correlation energy, and the Brillouin zone was sampled using a Monkhorst pack 6 × 9 × 5 *k*-point mesh, the plane-wave cut-off energy was set at 500 eV, and all the structural relaxation of the total energy was converged to 0.1×10^{-5} eV/atom.

3 Results and Discussion

The YSO and YSO:xPr^{3+} phosphors calcinated at 1650 °C were analyzed by the XRD, and the patterns of all phosphors were collected, as shown in Fig. 1(a). As presented, all the diffraction peaks of phosphors are in good agreement with the standard card of Y_2SiO_5 (JCPDS No. 97-002-8021) with the space group C2/c (Monoclinic), demonstrating that the target product pure phase Y_2SiO_5 is effectively synthesized independent of Pr^{3+} contents, as desired. Particularly, the XRD peaks gradually shift to the low-angle positions with an increase in Pr^{3+} concentration, as shown in magnified XRD patterns, signifying the expansion of the Y_2SiO_5 lattice interplanar spacing.

The schematic diagram of the Y_2SiO_5 crystal structure is depicted in Fig. 1(b). As presented, Y_2SiO_5 belongs to the monoclinic crystal structure with two distorted octahedral Y sites and one tetrahedral Si site. Two Y atoms coordinate with six O and seven O, respectively, to form the $Y1O_6$ octahedron and $Y2O_7$ decahedron, whereas the Si atoms coordinate with four oxygens to form the SiO_4 tetrahedra. The $Y1O_6$ octahedron and $Y2O_7$ decahedron are mutually connected by edge-sharing and meanwhile connected with SiO_4 tetrahedra via vertex-sharing. Therefore, the multi-site structure of Y_2SiO_5 provides a suitable doping site for Pr^{3+} ions.

Dopant ions can generally occupy the lattice sites of the host in the event of a modest maximal radius ratio of dopant ions to host ions (<30%). This radius ratio can be computed by the Eq. (1) [23]:

$$D = \frac{r_h - r_d}{r_h} \tag{1}$$

where r_h, and r_d refer to the ionic radii of the host ions and dopant ions in the same coordination case.

Access to literature, the ion radii of Y^{3+} (CN = 6) and Pr^{3+} (CN = 6) are 0.9 Å [24] and 0.99 Å [25], respectively. Analyzing the data reveals the radius ratios of Y^{3+} to Pr^{3+} of 10%, demonstrating that Pr^{3+} ions can successfully replace Y^{3+} sites in the Y_2SiO_5 host.

To obtain the precise crystallographic structure, the Rietveld refinements for YSO and YSO: xPr^{3+} phosphors were carried out using the basic structural model of monoclinic YSO (CSD No. 28021), as illustrated in Fig. 2. As presented, the observed curve, calculated curve, difference curve, and peak position could all be clearly seen. The Rietveld refinement results are reliable, as proved by the low values of R_{wp}, R_p, and χ^2. Analyzing the refinement data, the deeper crystal structure information is mined. As presented in Fig. 3 and Table 1, the variation in the lattice parameters (a, b, c, β, and volume) are depicted. It can be seen that the lattice parameters of a, b, c, β, and cell volume steadily increase as the Pr^{3+} concentrations rise from 0 to 0.2, signifying the expansion of crystal structure brought on by the substitution of Pr^{3+} ion for Y^{3+} ion. Based on the analysis mentioned above, it is shown that Pr^{3+} is successfully doped into the Y^{3+} site in the YSO host.

The typical band structure (BS) and electronic density of states (DOS) of the pure YSO matrix are computed by DFT. As presented in Fig. 4(a), it is found that the valence band maximum (VBM) and the conduction band minimum (CBM) are situated at the same G symmetry point of the Brillouin zone, indicating the YSO host is a direct band gap

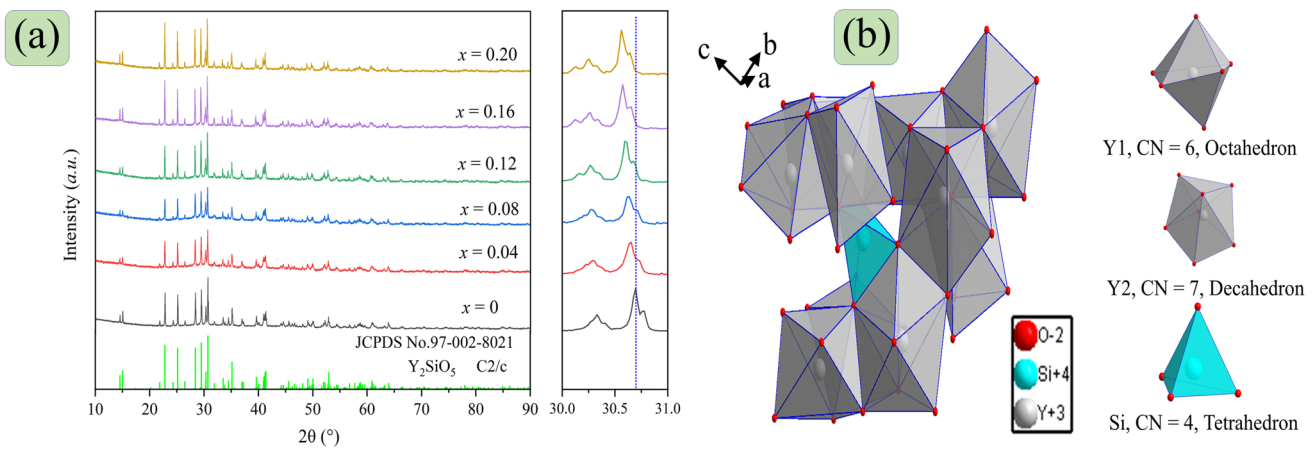

Fig. 1 **a** XRD patterns of YSO and YSO: xPr phosphors and (**b**) the crystal structure of the YSO

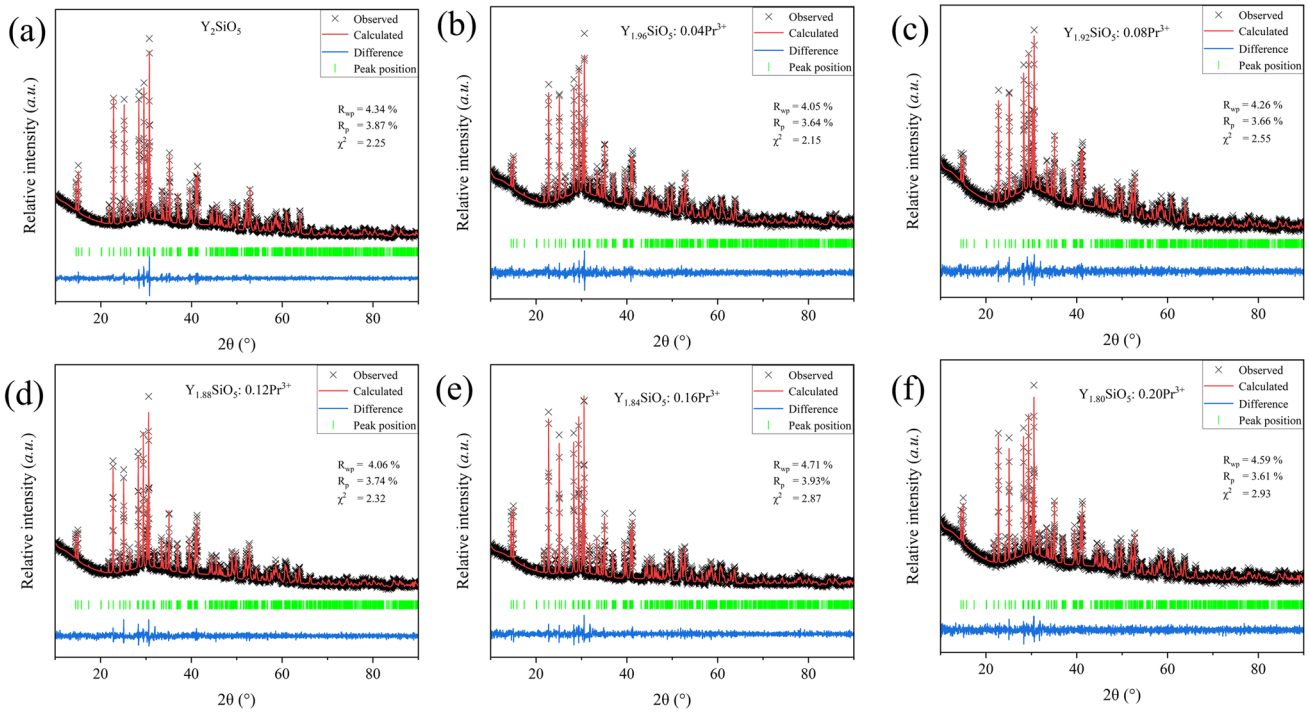

Fig. 2 Rietveld refinement for XRD of YSO and YSO: *x*Pr phosphors

insulator. Analyzing the data reveals the calculated band gap of 4.172 eV (i.e., the difference between CBM and VBM at the G point), this large value signifies that the band structure of the YSO host possesses a large band gap to accommodate the energy levels of the Pr^{3+} ions [26]. As shown in Fig .4(b), the total density of state (TDOS) and partial density of state (PDOS) at the ground state of the pure YSO matrix are portrayed. It can be found that the VB is mainly composed of Y-4*d*, Si-3*s*3*p*, and O-2*s*2*p* orbital, while the CB is mainly composed of Y-4*d*, Si-3*s*3*p* orbital. In addition, the VBM is dominated by the 2*p* state of O, while the CBM is dominated by the 4*d* state of Y, which indicates that the band gap of YSO is attributed to the charge transfer from the O-2*p* state to the Y-4*d* state [27].

The study of DRS helps to understand the optical transitions of luminescent materials. For this reason, the DRS of YSO and YSO: $x\mathrm{Pr}^{3+}$ phosphors were performed. As shown in Fig. 5(a), there is no absorption peak in the spectrum of the YSO host in the range of 400-800 nm, while two distinct absorption bands are identified in the spectra of YSO: $x\mathrm{Pr}^{3+}$ phosphors at the wavelength of 400-500 nm and 550-650 nm, respectively, which are attributed to the electron transitions of ${}^3H_4 \rightarrow {}^3P_2$ and ${}^3H_4 \rightarrow {}^1D_2$ for Pr^{3+} ion [20, 28]. With the increase of Pr^{3+} concentration, the intensities of absorption bands steadily enhance. Additionally, the absorption edges in DRS for all phosphors present a significant drop at around 250 nm, which may be due to the host absorption.

The band gap is one of the parameters that determine the application of phosphors in optoelectronic devices [29]. The band gap of powder samples can also be well determined using DSR with the following eqs. [30, 31]:

$$\left[\mathrm{F}\left(R_\infty\right)h\nu\right]^{\frac{1}{n}} = A\left(h\nu - E_\mathrm{g}\right) \tag{2}$$

$$\left[\mathrm{F}\left(R_\infty\right)\right] = \frac{\left(1-R_\infty\right)^2}{2R_\infty} \tag{3}$$

where $F(R_\infty)$ represents the Kubelka-Munk function, $h\nu$ is the photon energy, E_g refers to the band gap, and A means the constant. The n is a parameter associated with the electron transition types, the values of n are 1/2, 3/2, 2, and 3 for directly allowed transition, direct forbidden transition, indirect allowed transition, and indirect forbidden transition, respectively. In this work, the n is 1/2, as demonstrated by the DFT calculation.

The plot of $[\mathrm{F}(R_\infty)h\nu]$ [2] versus $h\nu$ is depicted in Fig. 5(b). The linear fitting region is extrapolated to the point where the ordinate is equal to 0, and the intercept of the abscissa is the value of E_g. Analyzing the data reveals the E_g values of 4.22 eV, 4.51 eV, 4.58 eV, 4.67 eV, 4.70 eV, and 4.72 eV, respectively. This result indicates that the E_g has been successfully modified by the doping of Pr^{3+} ions. Clearly, it is evident that the values are very close to the E_g (4.172 eV) calculated by DFT. Comparing the data from the

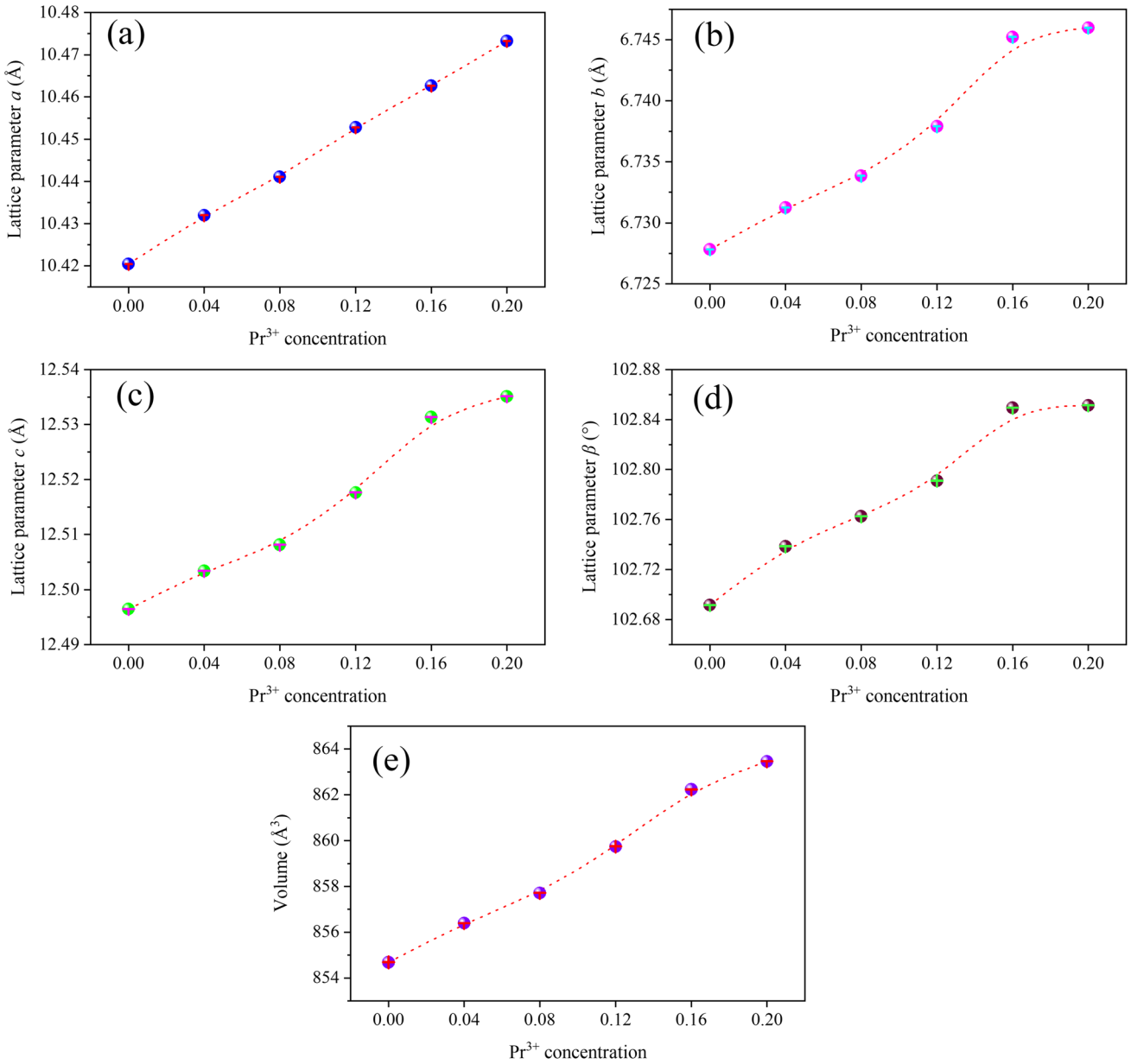

Fig. 3 The variation of crystal cell parameters and volume of the YSO: *x*Pr phosphors

two calculation methods, the E_g value determined by DFT calculation is underestimated, but this is a common feature of the DFT-based calculation [32].

To determine the crystal morphology characteristics of YSO: $x\text{Pr}^{3+}$ phosphors, the SEM images of the representative powder YSO:0.04Pr^{3+} were taken, as shown in Fig. 6. It can be found that the YSO:0.08Pr^{3+} phosphor calcinated at 1650 °C presents the irregular morphology, and the noticeable aggregation is found with an average grain size of 2 to 10 µm. The EDS elemental mapping images demonstrate that the Y, Si, Pr, and O elements are homogeneously distributed in the YSO:0.08Pr^{3+} phosphor.

Following testing, the emission spectra of YSO: $x\text{Pr}^{3+}$ calcinated at 1650 °C were tested and are portrayed in Fig. 7a. Under the excitation of 460 nm laser, two emission peaks centered at ~247 nm and ~ 258 nm are found and identified in the spectra of Pr^{3+}-doped YSO phosphors at the wavelength range of 230-280 nm, which are attributed to the transitions of $4f5d \rightarrow {}^3\text{H}_4$ and $4f5d \rightarrow {}^3\text{H}_5$ of Pr^{3+} ions [28, 33], respectively. In addition, the emission intensities of phosphors gradually rise with the increase of Pr^{3+} concentrations. At $x = 0.04$, the emission intensity of YSO: 0.04Pr^{3+} reaches the maximum, and then the intensity progressively declines with the Pr^{3+} concentrations further increasing,

Table 1 Refinement parameters for the YSO and YSO: *x*Pr phosphors

Formula	YSO (Experimental)	YSO: 0.04Pr	YSO: 0.08Pr	YSO: 0.12Pr	YSO: 0.16Pr	YSO: 0.20Pr
Space group	*C2/c*	*C2/c*	*C2/c*	*C2/c*	*C2/c*	*C2/c*
Symmetry	Monoclinic	Monoclinic	Monoclinic	Monoclinic	Monoclinic	Monoclinic
a (Å)	10.42046(25)	10.43199(19)	10.44105(31)	10.45280(20)	10.46264(19)	10.47325(35)
b (Å)	6.72783(10)	6.73125(12)	6.73386(22)	6.73791(16)	6.74522(11)	6.74599(19)
c (Å)	12.49644(14)	12.50341(15)	12.50814(35)	12.51761(11)	12.53137(20)	12.53515(21)
α = γ (°)	90	90	90	90	90	90
β (°)	102.6916(6)	102.7384(3)	102.7624(2)	102.7910(1)	102.8494(5)	102.8514(3)
Z	8	8	8	8	8	8
Volume(Å^3)	854.68(6)	856.39(1)	857.71(4)	859.74(8)	862.23(5)	863.46(3)
R_{wp} (%)	4.34	4.05	4.26	4.06	4.71	4.59
R_p (%)	3.87	3.64	3.66	3.74	3.93	3.61
χ^2	2.25	2.15	2.55	2.32	2.87	2.93

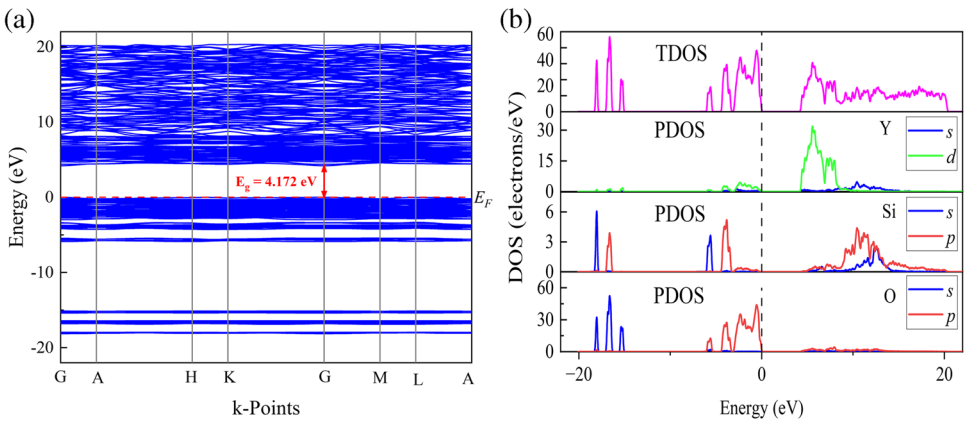

Fig. 4 **a** Band structure of YSO, (**b**) total and partial DOS in YSO

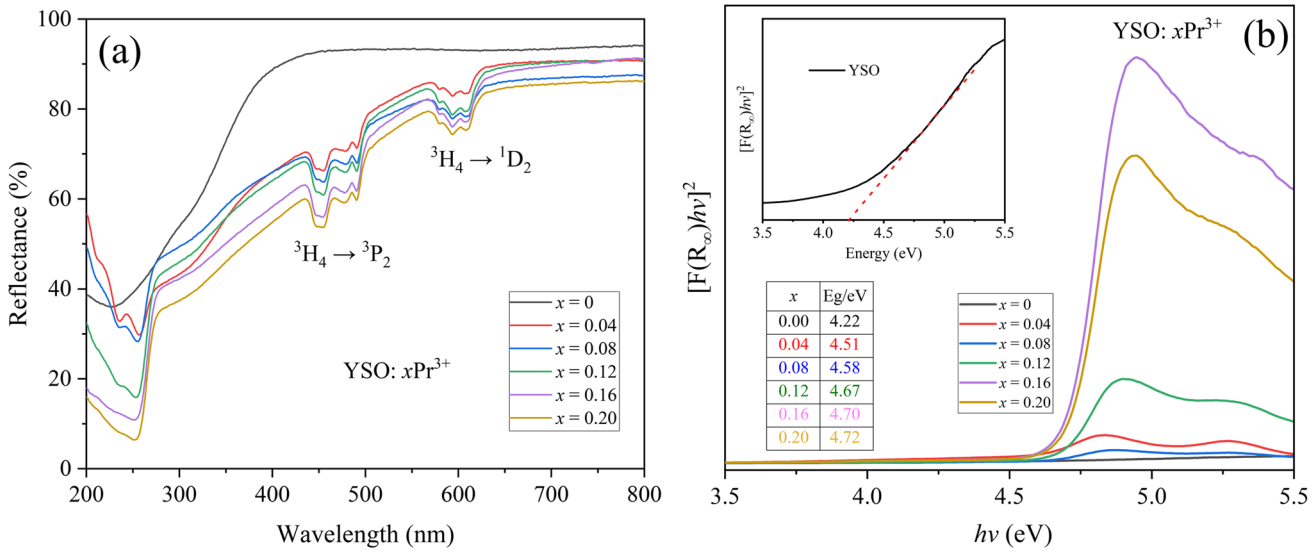

Fig. 5 **a** Diffuse reflection spectra of YSO and YSO: *x*Pr phosphors, (**d**) the relationship of $[F(R_\infty)h\nu]$ [2] versus $h\nu$

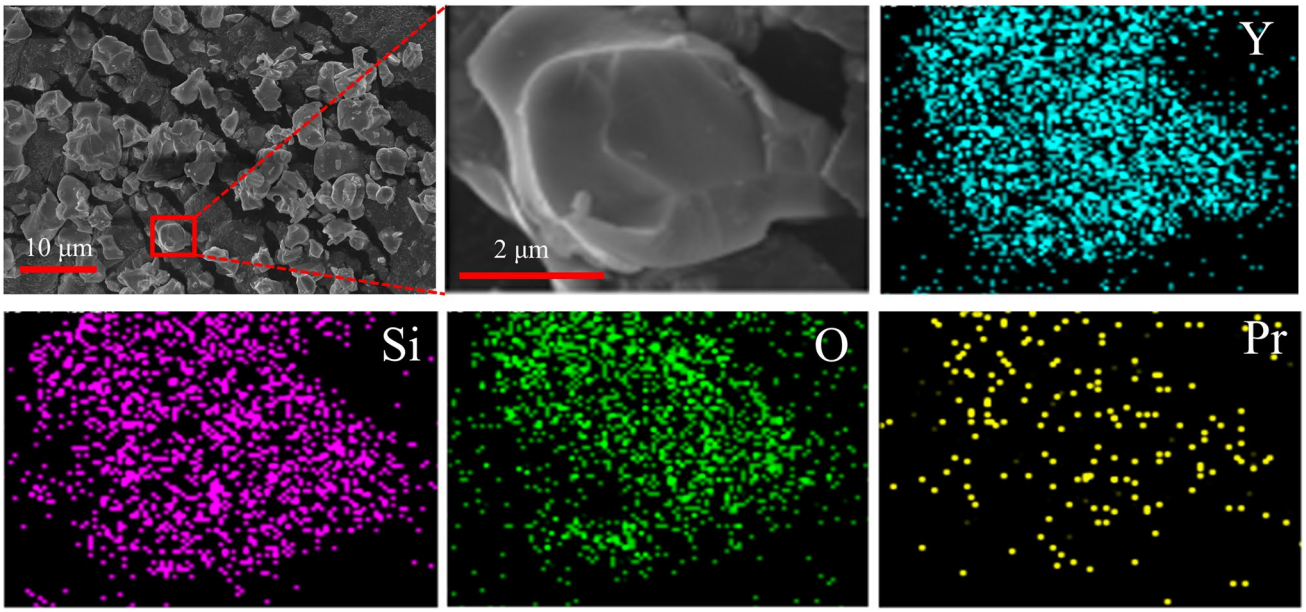

Fig. 6 SEM image, and EDS mapping of YSO: 0.08Pr phosphor

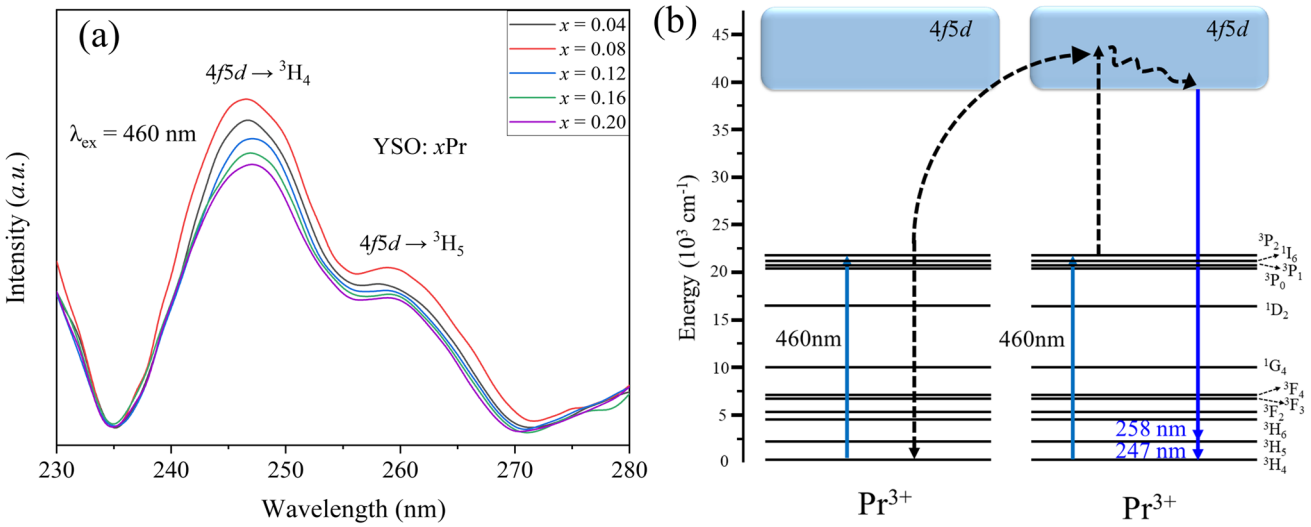

Fig. 7 **a** Emission spectra of YSO: xPr phosphors, and (**b**) schematic energy-level diagrams of Pr^{3+}

which may be due to the concentration quenching effect. The distance between the Pr^{3+} ions gets smaller than their critical separation, and the excitation energy is transferred to the energy killing center, which causes a reduction in the emission intensity of the YSO: Pr^{3+} phosphor [34, 35].

To explain the UVC upconversion luminescence of Pr^{3+} ions, the energy level diagrams and energy transfer mechanisms of Pr^{3+} ions are depicted in Fig. 7(b) [36]. As shown in Fig. 7(b), Upon the excitation of a 460 nm laser, the electrons of Pr^{3+} located in the $^3H_4$ ground state absorb 460 nm photons to jump to the $^3P_2$ state, the electrons populated $^3P_2$ state can then transit to the 4*f*5*d* level through absorbing another 460 nm photon via energy transfer process or excited-state absorption process. Next, the electrons of Pr^{3+} ions located in the 4*f*5*d* level will transit to the $^3H_4$ ground state and emit UVC light [18].

Figure 8 presents the fluorescence decay curves of YSO: xPr^{3+} phosphors excited at 460 nm laser and monitored at 247 nm. Here, all fluorescence decay curves for YSO: xPr^{3+} phosphors present a similar profile, and the artifact peaks are found at ~10 ns, which could be due to oscilloscope overshoot and is typical for this type of measurement [37,

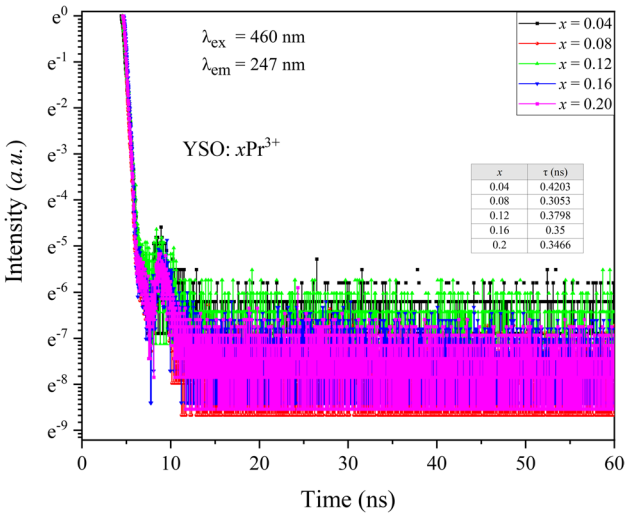

Fig. 8 Fluorescence decay curves of YSO: *x*Pr phosphors

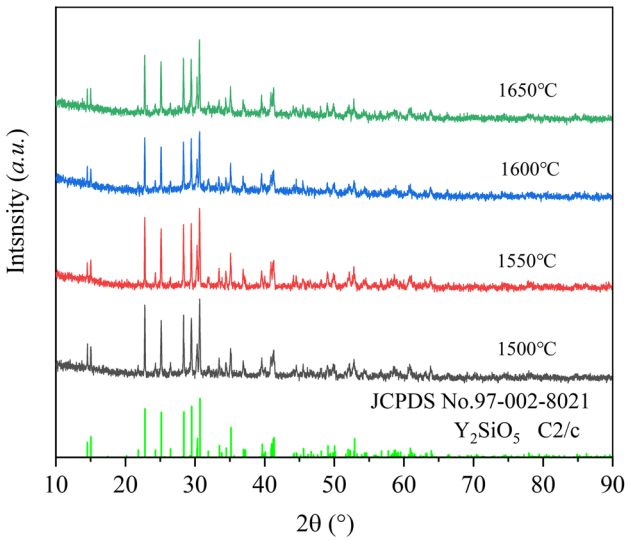

Fig. 9 XRD patterns of YSO: 0.08Pr phosphor calcinated at different temperatures

38]. Fitting the data, all the fluorescence decay curves can be fitted via the single-exponential function. Based on the analysis, the fluorescence decay lifetimes (τ) can be computed by the following equation [39]:

$$y = y_0 + A_1 \cdot \exp\left(-x/\tau_1\right) \tag{4}$$

where y_0 means the initial intensity of phosphors in decay curves, the y represents the intensity at x; A_1 is a constant.

Analyzing the data reveals the fluorescence decay lifetimes for all phosphors of 0.4203 ns, 0.3053 ns, 0.3798 ns, 0.3500 ns, and 0.3466 ns, respectively. Taking into account the measurement error, it may be assumed that the fluorescence lifetimes of all phosphors have no significant variation with the increase of Pr^{3+} concentrations.

It is well known that calcination temperature will have a certain influence on the structure and characteristics of phosphors during the solid phase sintering process. In this case, the XRD patterns of YSO:0.08Pr^{3+} phosphor calcinated at different temperatures were obtained, as shown in Fig. 9. It can be found that all XRD patterns have a similar profile, and all diffraction peaks match well with the standard card of Y_2SiO_5 (JCPDS No. 97-002-8021), which belongs to monoclinic crystal structure with the space group C2/c. In addition, examining the data reveals that pure YSO phase phosphors are successfully synthesized regardless of the calcination temperatures.

The emission spectra of YSO:0.08Pr^{3+} phosphor calcinated at different temperatures were tested and are depicted in Fig. 10(a). Under the excitation of 460 nm laser, there are two emission peaks centered at ~247 nm and ~258 nm in the region of 230-280 nm of the emission spectra of YSO:0.08Pr^{3+} phosphor, which display a similar profile and correspond to the transitions of $4f5d \rightarrow {}^3H_4$ and $4f5d \rightarrow {}^3H_5$ of Pr^{3+} ions. Observing the curves reveals the variation tendency of increasing first and then decreasing with an increase in calcination temperatures, and the integrated intensity of emission spectrum peaks at 1600 °C, as evidenced by the plot of normalized integrated intensity versus temperature (as shown in Fig. 10(b)). This may be explained by the following fact: the crystallinity of phosphor becomes better and better with the increase of calcination temperatures (≤1600 °C), which suppresses the non-radiative transition process of Pr^{3+} ions and improves the luminescent intensity of phosphor. In the case of 1600 °C, the luminescent intensity reaches a peak. Above 1600 °C, the crystallinity of the phosphor continued to increase, but the defects in the phosphor as well increased and the lattice of the powder is destroyed, thereby deteriorating the luminescent intensity of the phosphors [40].

For the application of phosphors, their thermal stability is a critical factor. In response to this situation, the temperature-dependent emission spectra of YSO:0.08Pr^{3+} were measured in the range of 25 to 200 °C. As shown in Fig. 11(a), the luminescent intensities continuously deteriorate as the increase of temperatures, which is due to the enhancement of non-radiative transition probability [41]. In fact, the increase in the sample's temperature leads to an increase in the lattice vibrations of the ions and thereby the enhancement of non-radiative transitions, which reduces the emission intensity of phosphor [42]. At 150 °C, the integrated emission intensity of phosphor can still contain 83.2% of the integrated intensity at room temperature (as shown in Fig. 11(b)). This high value at 150 °C demonstrates that the YSO: Pr^{3+} phosphors have good thermal stability at high temperatures.

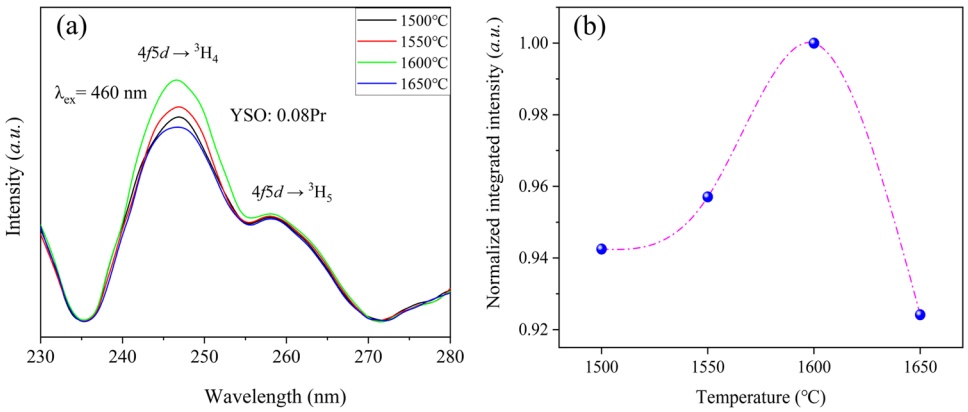

Fig. 10 **a** Emission spectra of YSO: 0.08Pr phosphor calcinated at different temperatures, and (**b**) normalized integrated intensities of emission spectra

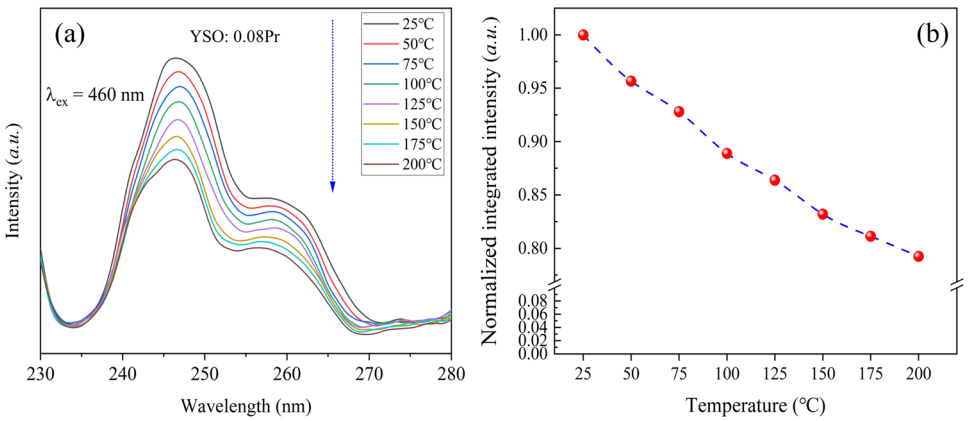

Fig. 11 **a** Temperature-dependent emission spectra of YSO: 0.08Pr calcinated at 1600 °C, and (**b**) integrated intensities of emission spectra

The fluorescence decay curves of YSO: 0.08Pr phosphors calcinated at different temperatures were also collected and are presented in (Fig. 12). Under the excitation at 460 nm laser and monitoring at 247 nm, the fluorescence decay curves of phosphors calcinated at different temperatures exhibit a similar profile as Pr^{3+}-doped phosphors YSO: $x Pr^{3+}$, meanwhile, the artifact peaks are also observed at ~10 ns. Fitting the date, the lifetimes of all phosphors are 0.3185 ns, 0.3838 ns, 0.3421 ns, and 0.3053 ns, respectively. In a comprehensive analysis, the lifetimes of phosphors are basically unchanged regardless of the calcination temperature.

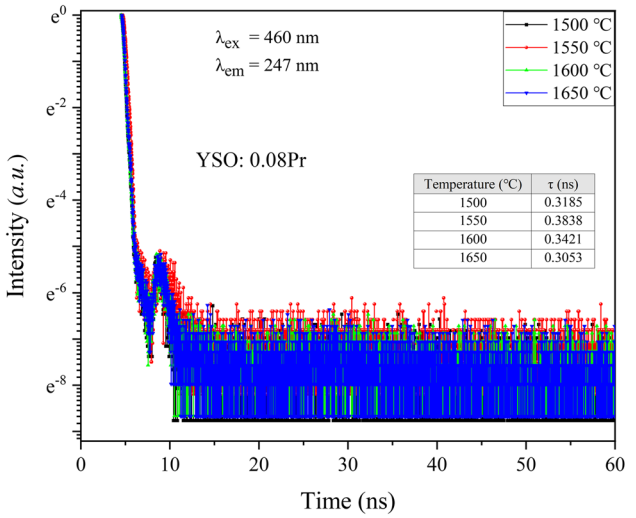

Fig. 12 Fluorescence decay curves of YSO: 0.08Pr phosphor calcinated at different temperatures

4 Conclusions

In summary, an efficient UVC-emitting upconversion phosphor $Y_2SiO_5:Pr^{3+}$ was successfully synthesized, as evidenced by the XRD results and the increase of the lattice parameters (a, b, c, β, and cell volume). The diffuse reflection spectra of $Y_2SiO_5:Pr^{3+}$ phosphors presented two absorption bands corresponding to the electron transitions of $^3H_4 \rightarrow {}^3P_2$ and $^3H_4 \rightarrow {}^1D_2$, and the E_g values of $Y_2SiO_5:xPr^{3+}$ were determined to be 4.22 eV, 4.51 eV, 4.58 eV, 4.67 eV, 4.70 eV, and 4.72 eV, which are very close to the E_g (4.172 eV) calculated by DFT. Based on SEM images and EDS elemental mapping images, the distinct aggregation was discovered with an average grain size of 2 to 10 μm, and Y, Si, Pr, and O elements were proven to be uniformly distributed in the YSO: Pr^{3+} phosphor. Under the excitation of 460 nm laser, two

emission peaks centered at ~247 nm and ~ 258 nm were discovered in the range of 230-280 nm, which are ascribed to the transitions of $4f5d \rightarrow {}^3H_4$ and $4f5d \rightarrow {}^3H_5$ of Pr^{3+} ions, respectively. With the aid of temperature-dependent emission spectra, the phosphors exhibited remarkable thermal stability up to 150 °C, and the integrated emission intensity of phosphor can still contain 83.2% of the integrated intensity at room temperature. These findings indicate that the Y_2SiO_5:Pr^{3+} phosphor has the potential application in disinfection.

Acknowledgments This work has been supported by the Science and Technology Program of Ganzhou city, Jiangxi Province ([2020]60), the Scientific Research Foundation for Universities from the Education Bureau of Jiangxi Province (GJJ210844, GJJ190453), the Jiangxi Provincial Training Program of Innovation and Entrepreneurship for Undergraduates (No. S202210407004), and the Jiangxi Provincial Natural Science Foundation of China (No. 20212BAB204023).

Authors' Contributions Fengqin Lai: Conceptualization, Methodology, Investigation, Writing–Original Draft. Xinning Xu: Conceptualization, Investigation, Writing–Original Draft. Junwei Shen: Investigation, Resources, Data Curation. Yuhang Wang: Validation, Investigation, Resources. Yinuo Yan: Conceptualization, Investigation, Resources. Yawen Nie: Resources, Data Curation. Weixiong You: Investigation. Di Wu: Investigation, Writing–review & editing, Project administration. Lei Han: Writing–review & editing, Project administration, Funding acquisition. Zongliang Xiao: Investigation, Resources, Data Curation, Funding acquisition.

Funding This work has been supported by the Science and Technology Program of Ganzhou city, Jiangxi Province ([2020]60), the Scientific Research Foundation for Universities from the Education Bureau of Jiangxi Province (GJJ210844, GJJ190453), the Jiangxi Provincial Training Program of Innovation and Entrepreneurship for Undergraduates (No. S202210407004), and the Jiangxi Provincial Natural Science Foundation of China (No. 20212BAB204023).

Data Availability All data generated or analyzed during this study are included in this published article.

Declarations

Ethics Approval The manuscript is prepared as per the ethical standard of the journal.

Consent to Participate Not applicable.

Consent for Publication The authors have given consent for publication as per the journal policy.

Conflict of Interest The authors declare that they have no known competing financial interests or personal relationships that could have appeared to influence the work reported in this paper.

References

1. Wang XL, Chen YF, Liu F, Pan ZW (2020) Solar-blind ultraviolet-C persistent luminescence phosphors. Nat Commun 11:2040
2. Weisman MJ, Dagefu FT, Moore TJ, Arslan CH, Drost RJ (2020) Analysis of the low-probability-of-detection characteristics of ultraviolet communications. Opt Express 28:23640
3. Buonanno M, Welch D, Shuryak I, Brenner DJ (2020) Far-UVC light (222 nm) efficiently and safely inactivates airborne human coronaviruses. Sci Rep 10:10285
4. Song K, Mohseni M, Taghipour F (2016) Application of ultraviolet light-emitting diodes (UV-LEDs) for water disinfection: a review. Water Res 94:341–349
5. Hou ZY, Zhang YX, Deng KR, Chen YY, Li XJ, Deng XR, Cheng ZY, Lian HZ, Li CX, Lin J (2015) UV-emitting upconversion-based TiO_2 photosensitizing nanoplatform: near-infrared light mediated in vivo photodynamic therapy via mitochondria-involved apoptosis pathway. ACS Nano 9:2584–2599
6. Nakahashi M, Mawatari K, Hirata A, Maetani M, Shimohata T, Uebanso T, Hamada Y, Akutagawa M, Kinouchi Y, Takahashi A (2014) Simultaneous irradiation with different wavelengths of ultraviolet light has synergistic bactericidal effect on Vibrio parahaemolyticus. Photochem Photobiol 90:1397–1403
7. Zhang Y, Luo YJ, Fu SQ, Lv XL, He Q, Ji FY, Xu X (2021) Visible-to-UVC driven upconversion photocatalyst sterilization efficiency and mechanisms of β-$NaYF_4$: Pr^{3+}, Li^+@BiOCl with a core-shell structure. J Environ Manag 288:112394
8. Kneissl M, Seong T, Han J, Amano H (2019) The emergence and prospects of deep-ultraviolet light-emitting diode technologies. Nat Photonics 13:233–244
9. Yadav RS, Verma RK, Bahadur A, Rai SB (2015) Infrared to infrared upconversion emission in Pr^{3+}/Yb^{3+} co-doped La2O3 and $La(OH)_3$ nano-phosphors: a comparative study. Spectrochim Acta, Part A 142:324–330
10. Yadav RS, Verma RK, Bahadur A, Rai SB (2015) Structural characterizations and intense green upconversion emission in Yb^{3+}, Pr^{3+} co-doped Y_2O_3 nano-phosphor. Spectrochim Acta, Part A 137:357–362
11. Yadav RS, Rai SB (2017) Frequency upconversion and downshifting emissions in solution combustion derived Yb^{3+}, Pr^{3+} co-doped strontium aluminate nano-phosphor: a multi-modal phosphor. J Lumin 190:171–178
12. Mi C, Zhou J, Wang F, Jin D (2019) Thermally enhanced NIR-NIR anti-stokes emission in rare earth doped nanocrystals. Nanoscale 11:12547–12552
13. Rabouw FT, Prins PT, Villanueva-Delgado P, Castelijns M, Geitenbeek RG, Meijerink A (2018) Quenching pathways in $NaYF_4$:Er^{3+}, Yb^{3+} upconversion nanocrystals. ACS Nano 12:4812–4823
14. Du YY, Ai XZ, Li ZY, Sun TY, Huang Y, Zeng XR, Chen X, Rao F, Wang F (2021) Visible-to-ultraviolet light conversion: materials and applications. Adv Photonics Res 2:2000213
15. Zheng KZ, Song WY, He GH, Yuan Z, Qin WP (2015) Five-photon UV upconversion emissions of Er^{3+} for temperature sensing. Opt Express 23:7653
16. Qin F, Zheng YD, Yu Y, Zheng CB, Liang HJ, Zhang ZG, Xu LL (2009) Ultraviolet upconversion luminescence in Er^{3+}-doped Y_2O_3 excited by 532 nm CW compact solid-state laser. J Lumin 129:1137–1139
17. Yin ZQ, Yuan P, Zhu Z, Li TY, Yang YM (2021) Pr^{3+} doped Li_2SrSiO_4: an efficient visible-ultraviolet C up-conversion phosphor. Ceram Int 47:4858–4863
18. Wu J, Zheng H, Liu X, Han B, Wei J, Yang Y (2016) UVC upconversion material under sunlight excitation: $LiYF_4$: Pr^{3+}. Opt Lett 41:792–795
19. Lin J, Su Q, Zhang HJ, Wang SB (1996) Crystal structure dependence of the luminescence of rare earth ions (Ce^{3+}, Tb^{3+}, Sm^{3+}) in Y_2SiO_5. Mater Res Bull 31:189–196

20. Hu CH, Sun CL, Li JF, Li ZS, Zhang HZ, Jiang ZK (2006) Visible-to-ultraviolet upconversion in Pr^{3+}: Y_2SiO_5 crystals. Chem Phys 325:563–566
21. Toby BH (2001) EXPGUI, a graphical user interface for GSAS. J Appl Crystallogr 34:210–213
22. Zhe FQ, Fa LC, Feng LZ, Wen ZZ, Xin C, Lin YC (2018) Distinct role of la doping in regulating the photo-oxidation and reduction of BiOBr nanosheet. Chinese J Inorg Chem 34:2115–2126
23. Liu Q, Xiong PX, Liu XQ, Fu YB, Wu S, Dong Q, Li YY, Chen Y, Ma ZJ, Peng MY (2021) Deep red $SrLaGa_3O_7$:Mn^{4+} for near ultraviolet excitation of white light LEDs. J Mater Chem C 9:3969–3977
24. Yang ZY, Zhao YF, Zhou YY, Qiao JW, Chuang YC, Molokeev MS, Xia ZG (2022) Giant red-shifted emission in (Sr, Ba)Y_2O_4:Eu^{2+} phosphor toward broadband near-infrared luminescence. Adv Funct Mater 32:2103927
25. Yin ZQ, Li MJ, Zhang JW, Shen Q (2021) Research on molecular structure and electronic properties of Ln^{3+} (Ce^{3+}, Tb^{3+}, Pr^{3+})/Li^+ and Eu^{2+} co-doped $Sr_2Si_5N_8$ via DFT calculation. Molecules 26:1849
26. Meng XD, Zhang GK, Li N (2017) $Bi_{24}Ga_2O_{39}$ for visible light photocatalytic reduction of Cr(VI): controlled synthesis, facet-dependent activity and DFT study. Chem Eng J 314:249–256
27. Sun ZS, Zhu ZP, Guo ZY, Wu ZC, Yang ZC, Zhang TT, Zhang XG (2019) Electronic structure and luminescent properties of Ce^{3+}-doped $Ba_3Lu_2B_6O_{15}$, a high-efficient blue-emitting phosphor. Ceram Int 45:7143–7150
28. Yin ZQ, Zhu Z, Lv PS, Zhang XF, Qi XW, Yang YM (2021) Luminescent properties of UVC up-conversion glassy phosphor: Li_2SrSiO_4 manufactured by containerless solidification. Mater Lett 291:129613
29. Dutta S, Som S, Priya J, Sharma SK (2013) Band gap, CIE and trap depth parameters of rare earth molybdate phosphors for optoelectronic applications. Solid State Sci 18:114–122
30. Xiao ZL, Ye JI, Wu BK, Wang FZ, Li JH, Zhang BH, Liu WZ, Han L, You WX (2022) Study on the influence of Bi^{3+} and Sm^{3+} doping on the luminescence properties of Ba_2SiO_4: Eu^{3+} red phosphor. Appl Phys A Mater Sci Process 128:120
31. Som S, Mitra P, Kumar V, Kumar V, Terblans JJ, Swart HC, Sharma SK (2014) The energy transfer phenomena and colour tunability in Y_2O_2S:Eu^{3+}/Dy^{3+} micro-fibers for white emission in solid state lighting applications. Dalton Trans 43:9860–9871
32. Li L, Pan Y, Zhou XJ, Zhao CL, Wang YJ, Jiang S, Suchocki A, Brik MG (2016) Luminescence enhancement in the $Sr_2ZnW_{1-x}Mo_xO_6$: Eu^{3+},Li^+ phosphor for near ultraviolet based solid state lighting. J Alloys Compd 685:917–926
33. Broxtermann M, den Engelsen D, Fern GR, Harris P, Ireland TG, Jüstel T, Silver J (2017) Cathodoluminescence and photoluminescence of YPO_4:Pr^{3+}, Y_2SiO_5:Pr^{3+}, YBO_3:Pr^{3+}, and YPO_4:Bi^{3+}. ECS J Solid State Sci Technol 6:R47–R52
34. Yadav RS, Dhoble SJ, Rai SB (2018) Enhanced photoluminescence in Tm^{3+}, Yb^{3+}, Mg^{2+} tri-doped ZnWO4 phosphor: three photon upconversion, laser induced optical heating and temperature sensing. Sensors Actuators B Chem 273:1425–1434
35. Yadav RS, Monika RSB, Dhoble SJ (2020) Recent advances on morphological changes in chemically engineered rare earth doped phosphor materials. Prog Solid State Chem 57:100267
36. Cates EL, Chinnapongse SL, Kim J, Kim J (2012) Engineering light: advances in wavelength conversion materials for energy and environmental technologies. Environ Sci Technol 46:12316–12328
37. Cates EL, Wilkinson AP, Kim JH (2015) Visible-to-UVC upconversion efficiency and mechanisms of $Lu_7O_6F_9$:Pr^{3+} and Y_2SiO_5:Pr^{3+} ceramics. J Lumin 160:202–209
38. Anker DS, Merkle LD (1999) Ion-ion upconversion excitation of the 4*f*5*d* configuration in Pr: $Y_3Al_5O_{12}$ experiments and Förster theory-based rate equation model. J Appl Phys 86:2933–2940
39. Song J, Zhang CY, Xu CY, Qiang YC, Lu AX, Han L (2022) Structure and luminescent properties of Eu^{3+}-doped phosphate glass for display device applications. Appl Phys A Mater Sci Process 128:629
40. Xiao ZL, Zhang Z, Li JH, Zhang BH, Wu BK, Wang FZ, Liu WZ, Song J, Han L, You WX (2021) Preparation and luminescent properties of $Y_2Zr_2O_7$:Eu^{3+} phosphor for W-LED application. Appl Phys A Mater Sci Process 127:866
41. Zhang XB, Zhang L, Xu YH, Wu XD, Yin SW, Zhong CS, You HP (2022) Broadband near-infrared-emitting phosphors with suppressed concentration quenching in a two-dimensional structure. Inorg Chem 61:7597–7607
42. Yadav RS, Kumar D, Singh AK, Rai E, Rai SB (2018) Effect of Bi^{3+} ion on upconversion-based induced optical heating and temperature sensing characteristics in the Er^{3+}/Yb^{3+} co-doped La_2O_3 nano-phosphor. RSC Adv 8:34699–34711

Publisher's Note Springer Nature remains neutral with regard to jurisdictional claims in published maps and institutional affiliations.

Springer Nature or its licensor holds exclusive rights to this article under a publishing agreement with the author(s) or other rightsholder(s); author self-archiving of the accepted manuscript version of this article is solely governed by the terms of such publishing agreement and applicable law.